ACCSCIENCE PUBLISHING

Engineering Science in Additive Manufacturing

ORIGINAL RESEARCH ARTICLE

Hot isostatic pressing temperature effects on the microstructure and mechanical properties of laser powder bed fusion-manufactured Hastelloy X

Bingqiu Wang[1], Rongrong Huang[1], Yiming Sun[2], Xiaohui Zhou[1], Linan Xue[2], Junjun Jiang[1], Swee Leong Sing[3], Bo Chen[1,4], Xiaoguo Song[1,4], and Caiwang Tan[1,4]*

[1]State Key Laboratory of Precision Welding and Joining of Materials and Structures, School of Materials Science and Engineering, Harbin Institute of Technology, Harbin, Heilongjiang, China

[2]Department of Welding and Materials Engineering, Beijing Power Machinery Institute, Beijing, China

[3]Department of Mechanical Engineering, College of Design and Engineering, National University of Singapore, Singapore

[4]School of Materials Science and Engineering, Shandong Institute of Shipbuilding Technology, Weihai, Shandong, China

Abstract

Hot isostatic pressing (HIP) of Hastelloy X alloy is an essential heat treatment process in manufacturing hot-end components for aerospace engines. This study investigated the microstructure evolution and mechanical properties of laser powder bed fusion-manufactured Hastelloy X superalloy at room and high temperatures under various HIP treatments. The results showed that as the HIP temperature increased, the recrystallization degree increased, with the proportion of low-angle grain boundaries decreasing from 49.7% at HIP1100 to 0% at HIP1210. The carbides along the grain boundaries evolved from particle distribution at HIP1100 to chain-like distribution at HIP1180 and coarsened at HIP1210. In the room temperature tensile test, specimens treated at HIP1100 exhibited the highest tensile strength due to restrained dislocation slip, grain refinement strengthening, and carbide dispersion strengthening. In the high-temperature tensile test, significant carbide coarsening was induced at HIP1100, while minimal changes were observed at HIP1180 and HIP1210. As the HIP temperature increased, the tensile strength and elongation both improved due to the synergistic effect of the reduced number of grain boundaries and chain-like distribution of carbides. The cracks primarily propagated along the grain boundaries, with the HIP1210 specimen showing a better capacity for crack inhibition.

Keywords: Hastelloy X superalloy; Laser powder bed fusion; High temperature tensile test; Microstructure; Carbide

***Corresponding author:**
Caiwang Tan
(tancaiwang@hitwh.edu.cn)

Citation: Wang B, Huang R, Sun Y, *et al*. Hot isostatic pressing temperature effects on the microstructure and mechanical properties of laser powder bed fusion-manufactured Hastelloy X. *Eng Sci Add Manuf.* 2025;1(2):025240015. doi: 10.36922/ESAM025240015

Received: May 14, 2025

Revised: June 20, 2025

Accepted: June 23, 2025

Published online: June 30, 2025

1. Introduction

Hastelloy X superalloy is a key structural material in the present aerospace industry due to its excellent high-temperature creep strength and exceptional corrosion

resistance.[1-3] As the core of aerospace vehicles, the turbofan engines encounter challenges such as complex structures, prolonged cycles, and high costs with casting and forging techniques.[4,5] Compared with traditional techniques, the laser powder bed fusion (LPBF) technology was employed to enable the integrated precision fabrication of complex structures.[6-8] However, the rapid layer-by-layer manufacturing process of as-built structures harmed the microstructure and mechanical properties, hindering the practical application of LPBF technology.[9,10] Therefore, heat treatment was necessary for as-built structures to enhance the comprehensive mechanical properties at room and high temperatures.[11-13]

Recently, to meet the application requirements of the above-mentioned specifications for Hastelloy X, the solution treatment was widely employed to optimize defects, homogenize the microstructure, and enhance mechanical properties. In research on room temperature mechanical properties, Keshavarzkermani *et al.*[14] analyzed the grain misorientation and grain boundary structure of as-built and solution-treated LPBF Hastelloy X samples. The result showed that the pores were eliminated, and grain recrystallization with varying degrees was induced with different solution treatment methods, accompanied by the columnar grains transforming into recrystallized equiaxed grains. Cheng *et al.*[15] investigated the strengthening mechanism between the microstructure and mechanical properties of the solution-treated Hastelloy X samples. They found that the full release of distortion energy with the complete grain recrystallization led to a significant reduction in the dislocation density and the appearance of twins. These studies succeeded in enhancing the mechanical properties at room temperature with limited grain anisotropy and twin boundary transition.

More importantly, the high-temperature mechanical properties of the Hastelloy X alloy are critical for the manufacturing of hot-end components for aerospace engines.[16-18] Montero-Sistiaga *et al.*[19] compared the high-temperature mechanical properties of as-built and solution-treated Hastelloy X specimens. They observed a substantial decline in both strength and ductility of the Hastelloy X alloy, which may be associated with carbide formation at the grain boundaries during the high-temperature tensile test. Agrawal *et al.*[20] also confirmed that the reduced ductility with the elevated temperature was attributed to the intergranular fracture caused by the carbides at the grain boundaries. Although the solution treatment of Hastelloy X alloy achieved high mechanical properties at room temperature, it failed to acquire sufficient mechanical properties in the high-temperature tensile test,[21] thereby impeding its practical application. Furthermore, it could be inferred that the low carbide content in the solution-treated Hastelloy X specimens restricted carbide formation and mechanical performance during high-temperature service. Therefore, it is imperative to devise a new heat treatment method to enhance the carbides of Hastelloy alloys.

In recent studies, hot isostatic pressing (HIP) has been considered a thermally activated process that promotes grain boundary migration and carbides with limited cooling rate.[22] A few studies reported that HIP treatment was beneficial for the enhancement of deformation capacity at high-temperature tensile tests.[23-25] It was found that the high-temperature deformation ability of HIP specimens was considered to be possibly affected by grain boundary proportion and carbide precipitation.[26-29] Marchese *et al.*[30] found that HIP-triggered recrystallization generated equiaxed grains, and the slow cooling rate led to the production of intergranular carbides and intragranular carbides in the 1160°C HIP process of Hastelloy X alloy. According to a report by Tomus *et al.*,[31] the low number of finely dispersed carbides segregating at the grain boundaries in the Hastelloy X alloy HIP-treated at 1,175°C showed minimal effect on its mechanical properties. Sanchez-Mata *et al.*[24] proposed that compared to discrete carbides along the grain boundaries under ST, HIP treatment at 1,155°C brought more continuous precipitates along grain boundaries in Hastelloy X specimens. Li *et al.*[32] proved that the chain-like and plate-like precipitates distributed at the grain boundaries under the HIP temperature of 1,100°C – 1,175°C contributed to the different mechanical properties of Hastelloy X specimens. Sun *et al.*[33] conducted HIP treatment at 1,050°C and solution treatment on LPBF-manufactured GH3536 alloy, with results showing that both tensile strength and elongation at high temperature were improved. In summary, the present HIP treatment temperature ranges from 1,050°C to 1,175°C for LPBF-manufactured Hastelloy X structures, based on casting and forging structures. However, a higher HIP temperature was required to activate the recrystallization and carbide precipitation process due to the distinctive microstructure characteristics, which are rarely reported in present studies. Therefore, by adopting elevated HIP temperature, this study primarily focused on the role of carbide control in enhancing the high-temperature mechanical properties of LPBF-manufactured Hastelloy X superalloy and the mechanism of grain recrystallization and carbides on mechanical performance following HIP treatment.

This study fabricated an LPBF as-built Hastelloy X specimen, along with those subjected to HIP treatment at 1,100°C, 1,180°C, and 1,210°C. The effects of HIP treatment on substructure, recrystallization, and carbide

characteristics were investigated, and mechanical properties at room and high temperatures were tested using failure mode analysis.

2. Experimental methods

2.1. Materials and deposition process

The Hastelloy X superalloy powder utilized in this experiment was gas atomized by Xi'an Bright Laser Technologies Co., Ltd (China). The composition of Hastelloy X superalloy powder is listed in Table 1.

The SLM280 machine produced by Solution GmbH in Germany was employed for LPBF. The laser focus diameter ranged from 80 μm to 115 μm. The experimental process was conducted under the protection of nitrogen, maintaining the proportion of oxygen below 0.2%. The pre-heat temperature of the substrate was set to 150°C to reduce the temperature gradient during the LPBF process. Before the LPBF process, the Magic24 software (version 24.0) was configured with the SLM280 to design the three-dimensional model of test samples, followed by importing the experiment parameters into SLM280 for setup. Based on the preliminary experiments, the experiment parameters for deposition were set at a laser power of 300W, scanning speed of 900 mm/s, and a layer rotation angle for scanning of 67°, as shown in Figure 1A.

The HIP treatment was conducted using the HIPEX850 HIP machine manufactured by CISRI HIPEX Technology CO., LTD. (China). The HIP machine utilized nitrogen as the pressure-transmitting medium, ensuring uniform pressure application on the component surface. According to the melting temperature of Hastelloy X alloy (1,295°C – 1,381°C), HIP treatments were performed at 1,100°C, 1,180°C, and 1,210°C, with a pressure of 160 MPa, a holding time of three hours, and a ventilation cooling rate of 4.5 K/min. The HIP specimens at 1,100°C, 1,180°C, and 1,210°C were labeled as HIP1100, HIP1180, and HIP1210, respectively.

2.2. Material characterization

The test specimens were cut from the LPBF-manufactured samples using wire electrical discharge machining, and the cross-sections were mechanically polished to achieve a smooth mirror finish. Aqua regia (hydrochloric acid: nitric acid: 3:1) was used to etch the cross-sectional surfaces of both the as-built and HIP specimens. The DSX510, manufactured by Olympus Corporation (Japan), was employed to observe the microstructural morphology and defects. The ImageJ software (version 1.53) was used to statistically analyze the rate of pores and carbides within a certain area.

The Zeiss's MERLIN Compact scanning electron microscope (SEM; Germany) was used for high-magnification microstructure observation. Energy dispersive spectroscopy integrated with the SEM was utilized for chemical composition analysis of the microstructure. After mechanical and electrolytic polishing to remove the strain layer, electron backscattered diffraction (EBSD) integrated with SEM was employed for microstructure characterization of the specimens. The TSL Orientation Imaging Microscopy analysis software (version 7.0) was used for the subsequent analysis of EBSD data.

The transmission electron microscopy (TEM) specimens were extracted from the central region of the as-built and HIP specimens. They were mechanically thinned to 60 μm using sandpaper, followed by ion milling. The ThemisZ spherical aberration-corrected TEM (Tecnai G2 F30, US) was used to analyze the substructure morphology and element distribution within the specimens.

After the sample surfaces were polished, the hardness of cross-sections of the as-built and HIP specimens

Table 1. Chemical composition of Hastelloy X

Element	Nickel	Ferum	Chromium	Molybdenum	Cobalt	Carbon	Tungsten	Silicon	Aluminum	Titanium
Content (wt.%)	Balance	18.86	21.16	9.78	2.20	0.067	0.62	0.037	0.028	<0.01

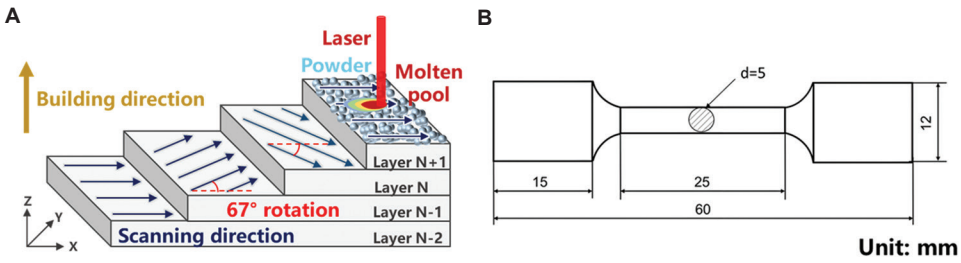

Figure 1. Schematic of building specimens. (A) A schematic diagram of the scanning strategy by laser powder bed fusion. (B) The profile of the tensile test specimen along the building direction.

was measured using Qness Q10 hardness tester (Qness, Austria), with a test load of 1 kg and a holding time of 10 s. Eight points were sampled along the central line in the building direction of each specimen. According to the GB/T 228.1-2010 standard, tensile tests at room temperature were conducted using the UTM5105X electronic universal material testing machine manufactured by SUNS (China). The tensile speed was set at 0.5 mm/min before yielding and 2.5 mm/min after yielding. The tensile test specimens were obtained by wire electrical discharge machining, and the dimensions of the tensile test specimens are shown in Figure 1B. Before the tensile test, the surfaces were polished to reduce the influence of surface roughness on the tensile properties.

Based on the average actual service temperature of hot-end components of aerospace engines manufacturing, high-temperature tensile tests at 900°C were conducted to investigate the effect of HIP temperature on high-temperature mechanical properties according to the GB/T 37783-2019 standard. The tests were performed using the SANS-CMT-52052 electronic universal testing machine (MTS Systems Corporation, China), with a tensile speed of 0.5 mm/min before yielding and 1.5 mm/min after yielding.

3. Results and discussion

3.1. Microstructures

Figure 2 presents the X-Y cross-sectional optical microscopy microstructural morphology of the as-built, HIP1100, HIP1180, and HIP1210 Hastelloy X specimens. The pores in the as-built specimen were observed at the edge of the obvious laser scanning tracks, as depicted in Figure 2A. However, the pores were effectively eliminated after the HIP treatments, and the laser scanning tracks completely disappeared at HIP1180 and HIP1210. The fine and coarse equiaxed grains were distributed at the edge and the center of the scanning tracks at HIP1100, respectively, as shown in Figure 2B. An uneven distribution of grain size was observed at HIP1180, as shown in Figure 2C. The finer equiaxed grains were engulfed by larger ones at HIP1210, resulting in a more uniform grain size distribution, as depicted in Figure 2D.

Figure 3 shows the EBSD results of the as-built, HIP1100, HIP1180, and HIP1210 specimens to investigate the microstructural evolution after various HIP treatments. The columnar grains in the as-built specimen were characterized by a small aspect ratio, with a length of 80 – 100 μm, corresponding to the set laser scanning spacing, as shown in Figure $3A_1$. In addition, the grains were observed with a maximum multiple of uniform density (MUD) value of 6.4, as depicted in Figure $3A_3$. After the HIP1100 treatment, the columnar grains of the as-built specimen transformed into equiaxed grains without a specific grain orientation, accompanied by a MUD value of 4.834, as shown in Figure $3B_1$ and B_3. At HIP1180 and HIP1210, the MUD values decreased to 2.915 and 3.487, respectively, indicating that the texture in the as-built specimen was almost eliminated, as depicted in Figure $3C_1$, C_3, D_1, and D_3. Therefore, it could be inferred that as the HIP temperature increased, a random grain orientation was achieved and the microstructure anisotropy was restrained.

Moreover, the angle distribution of the grain boundary changed, as shown in Figure $3A_2$, B_2, C_2, and D_2. Low-angle grain boundaries were observed in the as-built specimen, accounting for 51.5% (the ratio of low-angle grain boundary length to the total grain boundary length), as shown in Figure $3A_2$. This indicated the presence of a large number

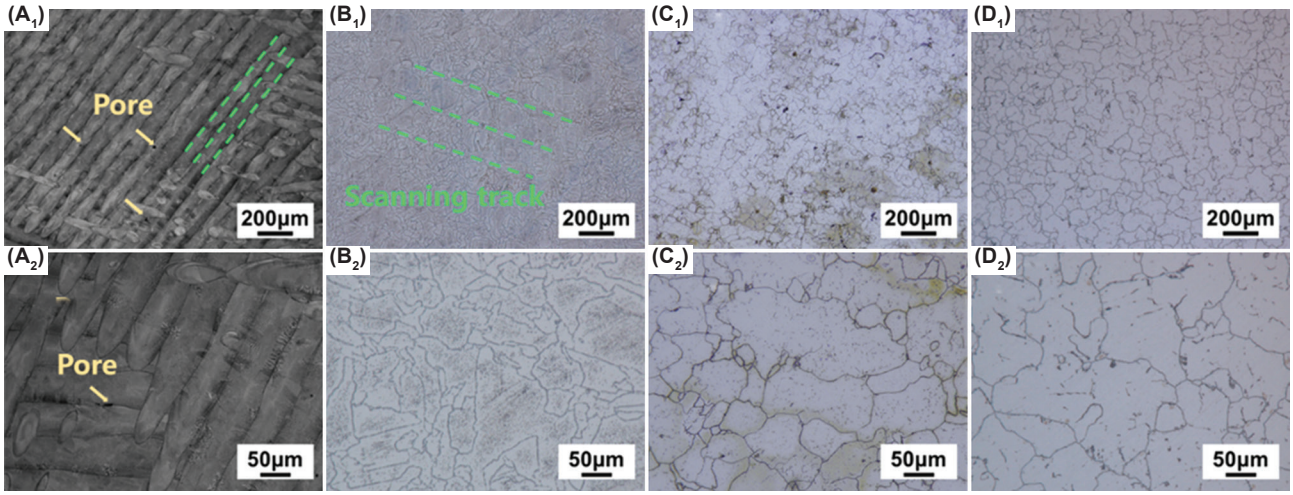

Figure 2. Optical microscopy microstructural morphology and local magnified region of (A_1 and A_2) as built, (B_1 and B_2) HIP1100, (C_1 and C_2) HIP1180, and (D_1 and D_2) HIP1210 specimens. Scale bar: 50 μm, magnification: (A_1-D_1) ×200; (A_2-D_2) ×1,000.
Abbreviation: HIP: Hot isostatic pressing.

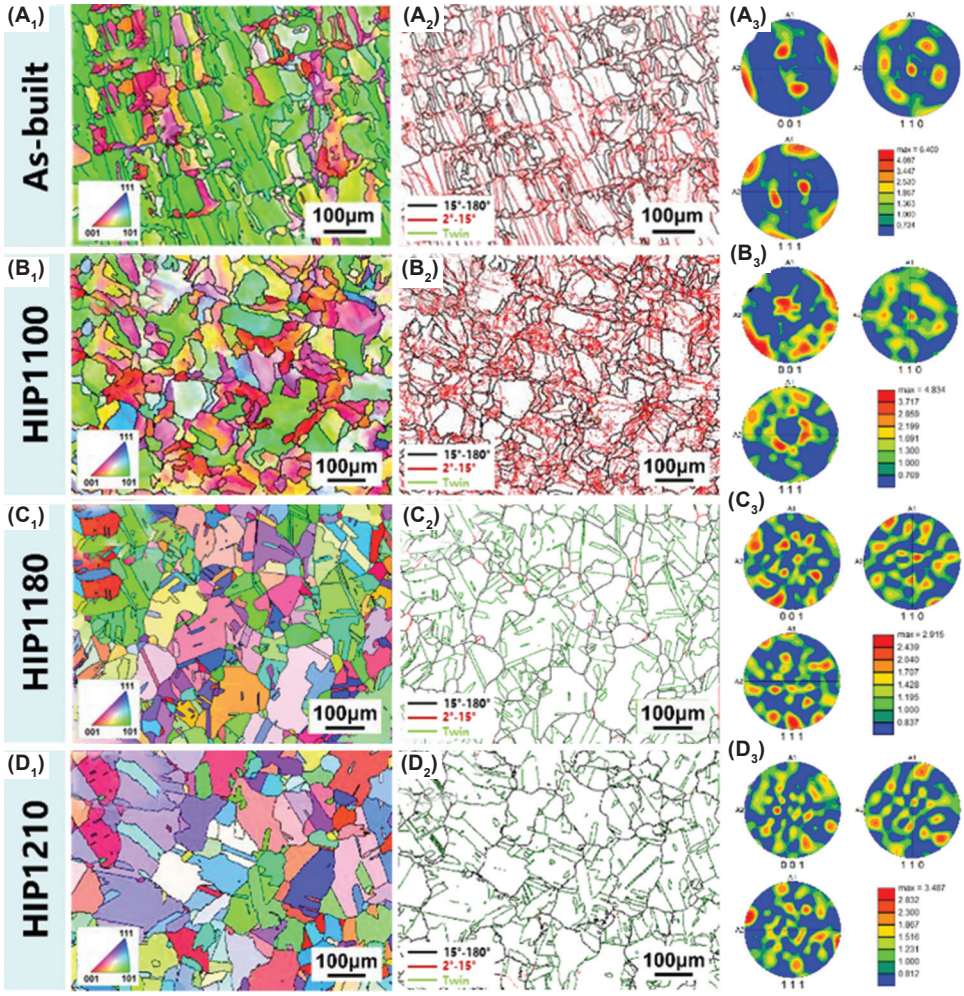

Figure 3. Electron backscattered diffraction results of the as-built, HIP1100, HIP1180, and HIP1210 specimens. (A_1, B_1, C_1, and D_1) Inverse pole figure maps, (A_2, B_2, C_2, and D_2) grain boundary maps, and (A_3, B_3, C_3, and D_3) pole figure map. Scale bar: 100 μm, magnification: ×500.
Abbreviation: HIP: Hot isostatic pressing.

of substructure boundaries, accompanied by high-density dislocations. Numerous low-angle grain boundaries were also observed at HIP1100, with the proportion decreasing to 49.7%, suggesting that the substructures remained, as shown in Figure $3B_2$. At HIP1180, the low-angle grain boundaries almost disappeared with a proportion of 4.3%, as displayed in Figure $3C_2$. In addition, a large number of annealing twins appeared and were measured at approximately 31% (the ratio of twin boundary length to the total grain boundary length), the low interface energy of which was beneficial for alleviating the stress concentration within the specimen. At HIP1210, the low-angle grain boundaries were completely replaced by the high-angle grain boundaries and twin boundaries, as displayed in Figure $3D_2$.

To intuitively characterize the grain recrystallization under different HIP treatments, the EBSD data were processed, and the kernel average misorientation map was employed to mark the recrystallized grains by setting a specific range for local strain, as shown in Figure $4A_1$, B_1, C_1, and D_1. The as-built specimen showed minimal recrystallization, while more recrystallization occurred in the HIP specimens. At HIP1100, the incomplete recrystallization of the Hastelloy X specimen was observed, with recrystallized grains accounting for 43% of the total. At HIP1180 and HIP1210, 98% and 100% of the equiaxed grains underwent recrystallization, respectively, indicating that the recrystallization process was almost completed. The diagrams of grain size distribution were statistically analyzed in Figure $4A_2$, B_2, C_2, and D_2. In the as-built specimen, the grain size was below 60 μm, with an average value of 16.4 μm. At HIP1100, a large number of microstructure characteristics in the as-built specimen were retained with an average grain size of

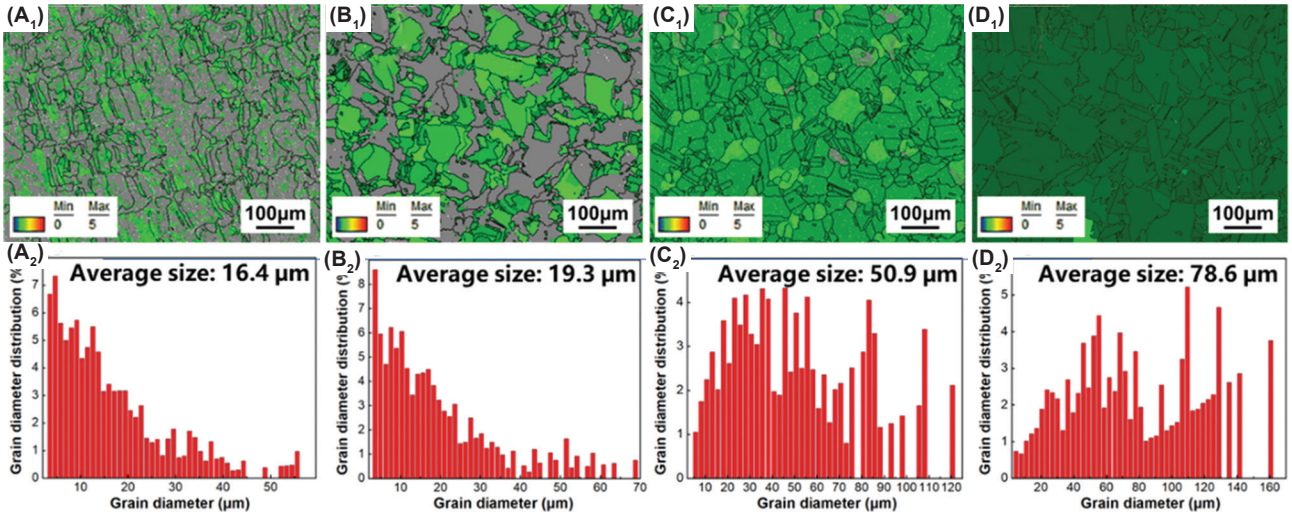

Figure 4. Kernel average misorientation map and the corresponding diagrams of grain size distribution. Results of (A_1 and A_2) as built, (B_1 and B_2) HIP1100, (C_1 and C_2) HIP1180, and (D_1 and D_2) HIP1210 specimens. Scale bar: 100 μm, magnification: ×500.
Abbreviation: HIP: Hot isostatic pressing.

19.3 μm. At HIP1180, the microstructure transitioned into the stage of complete recrystallization, leading to an increase in the average grain size to 50.9 μm. At HIP1210, the average grain diameter developed to 78.6 μm due to grain engulfment. In summary, the grain recrystallization process was prompted as the HIP temperature increased, accompanied by the microstructure transformation from the fine columnar grains to coarse equiaxed grains.

To investigate phase evolution within the grains and along the grain boundaries, the SEM morphology of carbides in HIP1100, HIP1180, and HIP1210 specimens was examined, and the corresponding diagrams of carbide size distribution are presented in Figure 5. In all HIP-treated specimens, white precipitates were observed both intragranularly and along grain boundaries. This can be attributed to the extended holding time with the carbide precipitation temperature range during the HIP soaking process, compared to the as-built specimen, which promoted more extensive carbide precipitation.[34] At HIP1100, carbides were distributed within the grains and also appeared as discrete particles along the grain boundaries, as depicted in Figure $5A_1$-A_4. In addition, it was found that the carbide size predominantly ranged from 0.05 μm to 0.2 μm with an average size of 0.279 μm. As the HIP temperature increased to 1,180°C, the carbides inside the grains partially dissolved, while carbides along the grain boundaries distributed continuously with a chain-like pattern, as shown in Figure $5B_1$-B_4. In addition, the average size of carbides increased to 0.40 μm. At HIP1210, the carbides within the grains completely disappeared, while those at the grain boundaries coarsened to envelop the entire grain, accompanied by an average size of 0.41 μm, as shown in Figure $5C_1$-C_4.

When the HIP temperature increased from 1,100°C to 1,210°C, the solubility of the solute element carbon in nickel within the Hastelloy X alloy decreased,[35] contributing to the enhanced precipitation of carbides. This resulted in an increase in the average carbide size. Moreover, during the HIP treatments, the loose structure of the grain boundaries served as a rapid diffusion pathway for solute elements,[36] leading to a higher precipitation rate of carbides along grain boundaries compared to within the grains. Consequently, carbides segregating along the grain boundaries exhibited larger sizes. At HIP1100, the distribution of dispersed carbides within the grains and particle carbides at the grain boundaries was attributed to the limited diffusion capability of the solute elements. At HIP1180, both the carbide re-dissolution within the grains and the carbide accumulation along the grain boundaries were prompted by the enhanced diffusion capability of the solute elements. As the HIP temperature increased to 1,210°C, intragranular carbides were completely re-dissolved, while extensive diffusion of solute elements led to significant coarsening of carbides along grain boundaries.

Different types and distribution patterns of carbides contribute differently to the strengthening of mechanical properties.[37,38] To further study the carbide characteristics following HIP treatments, the TEM morphology, selected area electron diffraction map, and energy dispersive spectroscopy map of carbides in the HIP1180 specimen are displayed in Figure 6. The chain-like carbides exhibited dimensions exceeding 1 μm in length and 60 nm in width, as shown in Figure 6A and B. The carbides were identified as M_6C (rich in molybdenum) and $M_{23}C_6$ (rich in chromium), as shown in Figure 6C. An interspersed distribution of

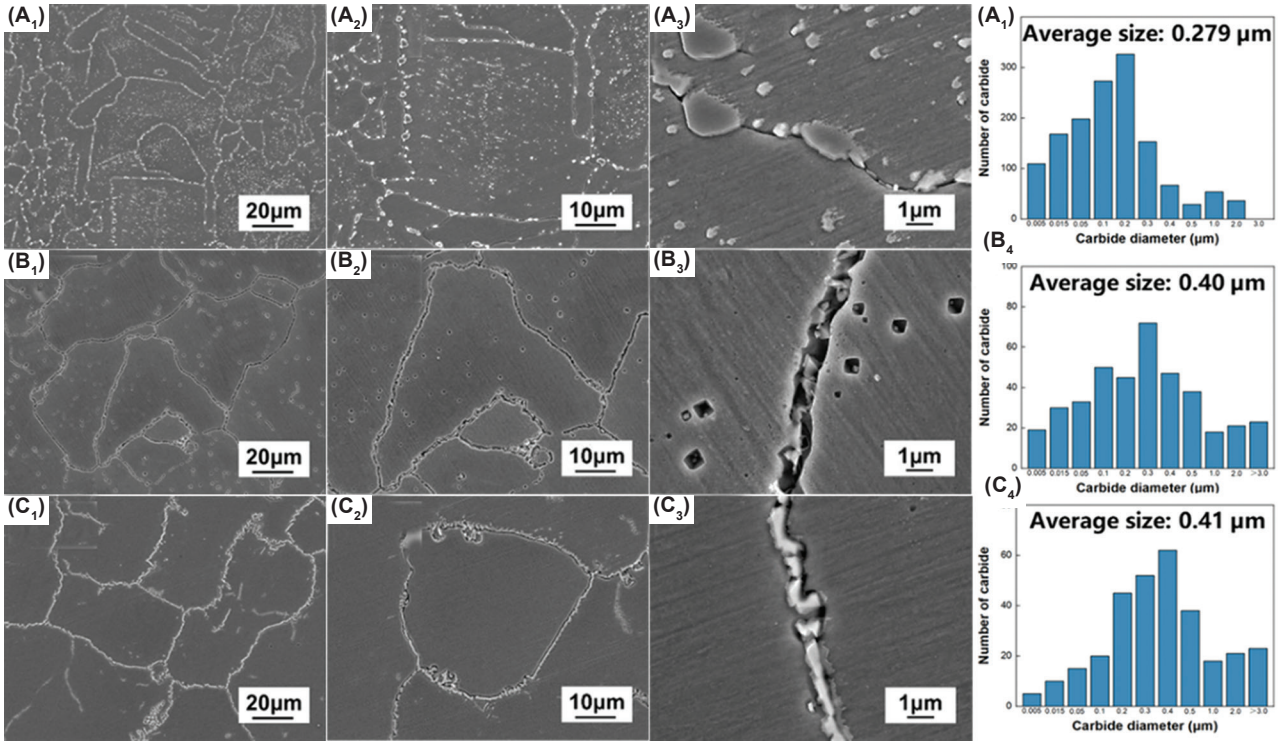

Figure 5. Carbide morphology and the corresponding diagrams of carbide size distribution. Results of (A_1-A_4) HIP1100, (B_1-B_4) HIP1180, and (C_1-C_4) HIP1210 specimens. Scale bars: (A_1-C_1) 20 μm; (A_2-C_2) 10 μm; (A_3-C_3) 1 μm, magnifications: (A_1-C_1) ×2,000; (A_2-C_2) ×5,000; (A_3-C_3) ×30,000.
Abbreviation: HIP: Hot isostatic pressing.

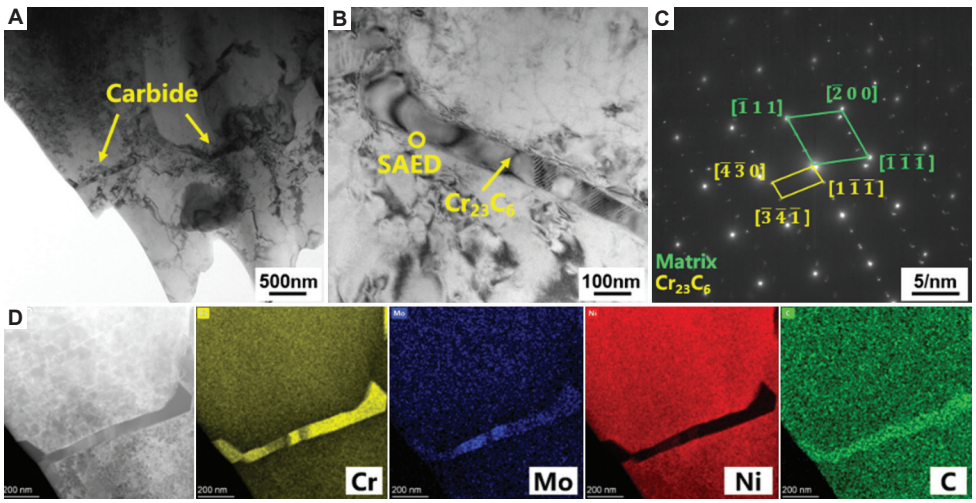

Figure 6. Transmission electron microscopic morphology of carbides in the HIP1180 specimen. (A and B) carbide morphology and local magnified region, (C) selected area electron diffraction, and (D) energy dispersive spectroscopy mapping profile of carbides. Scale bars: (A) 500 nm; (B) 100 nm; (C) 5 nm; (D) 200 nm, magnifications: (A) ×60,000; (B) ×300,000; (C) ×300,000; (D) ×150,000.
Abbreviations: C: Carbon; Cr: Chromium; Mo: Molybdenum; Ni: Nickel; HIP: Hot isostatic pressing.

the carbides consisting of M_6C and $M_{23}C_6$ was observed along the grain boundaries, as depicted in Figure 6D. This distribution pattern is attributed to the simultaneous precipitation of both carbide types in various areas, followed by preferential growth along grain boundaries.

3.2. Mechanical properties at room temperature

A comparison of the hardness of the as-built, HIP1100, HIP1180, and HIP1210 specimens is shown in Figure 7A. The as-built specimen exhibited the highest hardness with a value of 268 HV, while the HIP1100, HIP1180,

and HIP1210 specimens demonstrated hardness values of 244.24 HV, 214.42 HV, and 211.44 HV, representing a decline of 8.9%, 20.0%, and 21.1%, respectively. This could be attributed to the progressed recrystallization process with the elevated HIP temperature. The substructures gradually vanished, accompanied by a reduction in the number of low-angle grain boundaries, as depicted in Figure 3. Therefore, the hindrance for substructures to dislocation slip is reduced, leading to a decline in hardness.

Tensile tests of all specimens at room temperature were conducted, and the results are presented in Figure 7B. Compared to the as-built specimen, the tensile strength and elongation of the HIP specimens improved, while the yield strength decreased. The improvement of tensile strength of HIP specimens was achieved due to the reduction of porosity through the HIP treatment. In addition, as the HIP temperature increased, the elongation gradually improved, reaching a maximum value of 45% at HIP1210, while the yield strength and tensile strength declined. The HIP specimen, HIP1100, achieved the highest yield strength of 569 MPa and the highest tensile strength of 774 MPa, which was associated with the synergistic effect of the dislocation slip, grain size, and carbide distribution. On one hand, dislocation slip was effectively hindered at HIP1100 due to a higher proportion of low-angle grain boundaries compared to HIP1180 and HIP1210. On the other hand, the presence of fine grains and small, dispersed particle carbides contributed to grain refinement strengthening and dispersion strengthening, respectively.

Figure 8 presents the fracture surfaces of the as-built, HIP1100, HIP1180, and HIP1210 tensile specimens tested at room temperature. Cracks were observed on the fracture surfaces of the HIP1180 and HIP1210 specimens. This cracking is attributed to the precipitation and

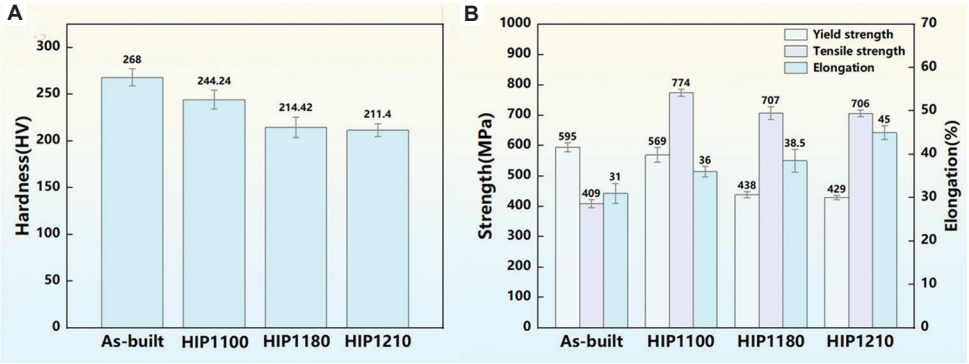

Figure 7. Mechanical properties obtained at room temperature of as-built, HIP1100, HIP1180, and HIP1210 specimens. (A) Microhardness and (B) Yield strength, tensile strength, and elongation.
Abbreviation: HIP: Hot isostatic pressing.

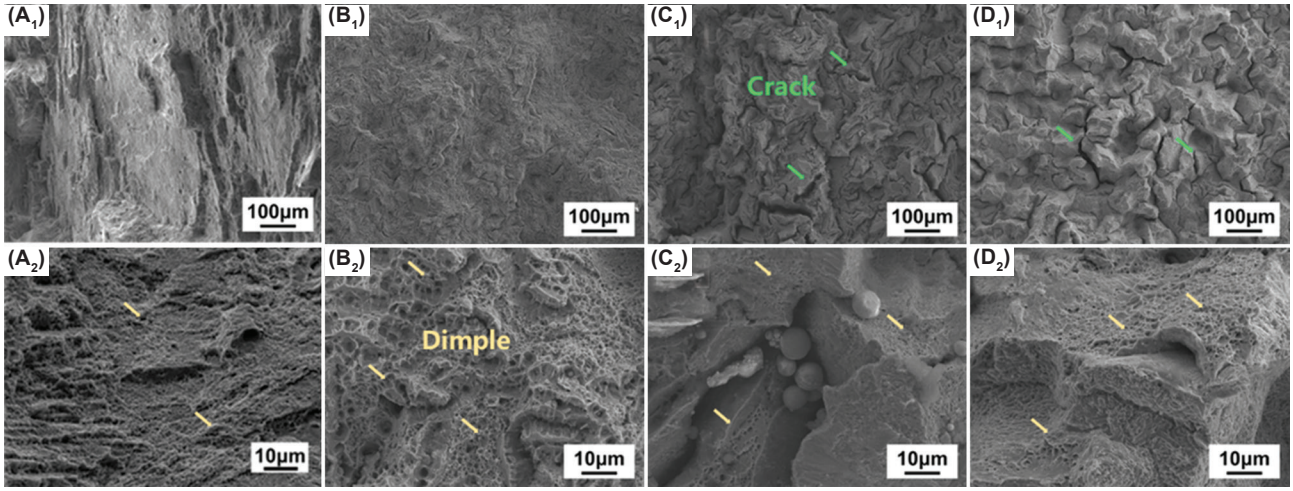

Figure 8. Fracture surfaces of Hastelloy X tensile specimens failed at room temperature. Results of (A_1 and A_2) as-built, (B_1 and B_2) HIP1100, (C_1 and C_2) HIP1180, and (D_1 and D_2) HIP 1210 specimens. Scale bars: (A_1-D_1) 100 μm; (A_2-D_2) 10 μm, magnifications: (A_1-D_1) ×500; (A_2-D_2) ×5,000.
Abbreviation: HIP: Hot isostatic pressing.

coarsening of carbides along the grain boundaries, which eventually envelop the grains and increase the brittleness of the grain boundaries, as shown in Figure 5. During subsequent plastic deformation, the secondary cracks were induced through crystal fractures.[39] Furthermore, higher magnification images revealed numerous dimples in the fracture surface of all specimens, proving that the tensile failure mode at room temperature was characteristic of ductile fracture.

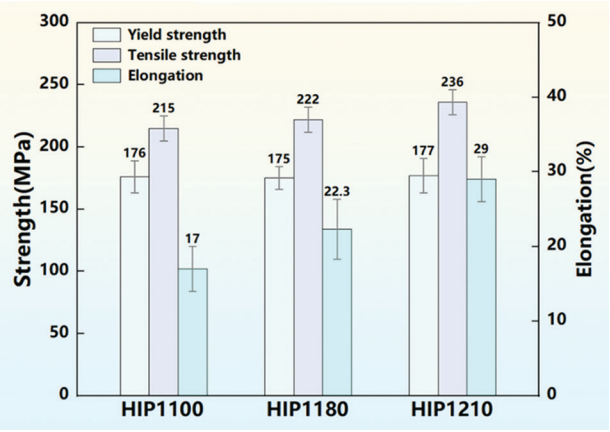

Figure 9. The yield strength, tensile strength, and elongation obtained at high temperatures for HIP1100, HIP1180, and HIP1210 specimens
Abbreviation: HIP: Hot isostatic pressing.

3.3. Mechanical properties at high temperature

To evaluate high-temperature mechanical properties, the tensile results of HIP specimens at 900°C are presented in Figure 9. As reported in recent studies,[19-21,40] HIP treatment significantly improved the high-temperature mechanical properties compared to the as-built condition. The yield strength, tensile strength, and elongation obtained in the high-temperature tensile test were lower than those at room temperature. As HIP temperature increased, the yield strength exhibited no significant changes, while the elongation gradually increased, reaching a maximum value of 29.0% at HIP1210. Interestingly, the trend for tensile strength at high temperature differed from that observed at room temperature. The tensile strength of the specimen at HIP1210 reached 236 MPa, representing an improvement of 9.8% and 6.3% compared to the HIP1100 and HIP1180 specimens, respectively.

The carbide morphology within the high-temperature deformation region and the statistical diagrams of carbide size distribution of HIP1100, HIP1180, and HIP1210 specimens are displayed in Figure 10. After the

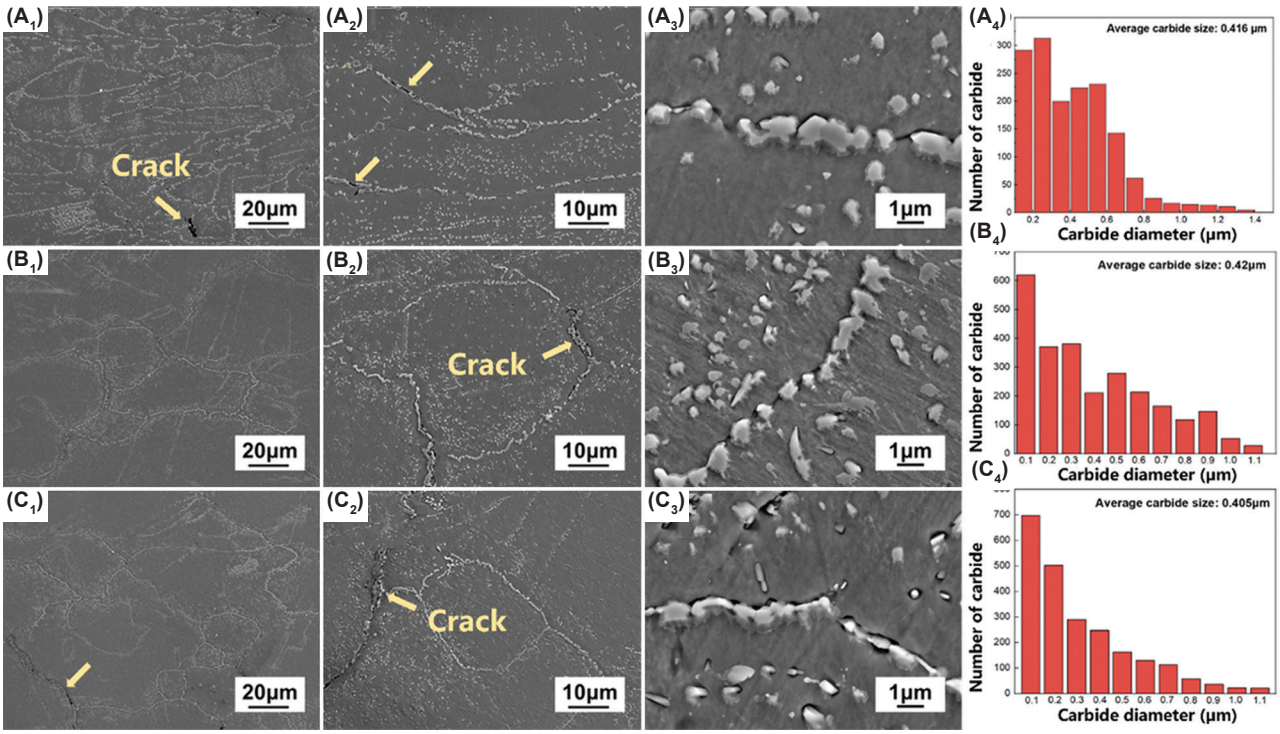

Figure 10. The carbide morphology of the deformation region failed at high tensile temperature, and the corresponding diagrams of carbide size distribution. Results of (A_1-A_4) HIP1100, (B_1-B_4) HIP1180, and (C_1-C_4) HIP1210 specimens. Scale bars: (A_1-C_1) 20 μm; (A_2-C_2) 10 μm; (A_3-C_3) 1 μm, magnifications: (A_1-C_1) ×2,000; (A_2-C_2) ×5,000; (A_3-C_3) ×30,000.
Abbreviation: HIP: Hot isostatic pressing.

high-temperature tensile test, cracks were observed in areas enriched with carbides along the grain boundaries of all specimens. The average carbide size of the HIP1100 specimen increased from 0.279 μm to 0.416 μm, as shown in Figure 10A_1-A_4. Moreover, the carbide distribution along the grain boundaries transformed from particle distribution to bulk distribution. However, the average carbide size at both HIP1180 and HIP1210 showed minimal changes compared to that of room temperature, as shown in Figure 10B_1-B_4 and C_1-C_4. Furthermore, carbides were observed within the grains in the HIP1180 and HIP1210 specimens. However, the carbides at the grain boundaries exhibited a chain-like distribution, with a higher concentration on grain boundaries compared to within the grains.

Figure 11 illustrates the microstructural morphology and the local magnified region of the deformation region failed at the 900°C tensile test of HIP specimens. Long cracks penetrating the tensile specimen were observed in the HIP1100 specimen, as shown in Figure 11A_1-A_3. In the HIP1180 specimen, the wedge cracks were confined solely to a local region, as presented in Figure 11B_1-B_3. In comparison with the HIP1100 and HIP1180 specimens, crack formation in the HIP1210 specimen was effectively suppressed, with cracks appearing smaller, as depicted in Figure 11C_1-C_3. In addition, most cracks occurred and propagated along the grain boundaries due to its brittleness.

Figure 12 illustrates the fracture surface of HIP tensile specimens at high-temperature deformation. Part of the characteristics of laser scanning morphology were retained on the fracture surface at HIP1100, accompanied by obvious cracks, as shown in Figure 12A_1 and A_2. The fracture surface of HIP1180 exhibited a pronounced massive pattern morphology, which corresponded to the brittleness of the grain boundaries, as shown in Figure 12B_1 and B_2. Compared to the HIP1100 and HIP1180 specimens, this massive feature was even more prominent in the HIP1210 specimen, demonstrating a typical characteristic of intergranular fracture, as presented in Figure 12C_1 and C_2.

Based on the above analysis, the high-temperature fracture mechanisms of the HIP specimens are presented in Figure 13. During the 900°C tensile test, carbides continued to precipitate and coarsen in the HIP specimens. Due to the enhanced diffusion capability of solute elements in the high-temperature tensile test,[37] these elements exhibited a propensity to segregate into regions of high-density dislocations and grain boundaries, promoting carbide precipitation and coarsening in those areas. Therefore, the growth rate of carbides was higher at the grain boundaries than within the grains. Due to the short duration of the high-temperature tensile test, variations in carbide morphology among the different HIP specimens were primarily governed by their morphology before deformation. In the HIP1100 specimen, the presence of numerous vacancies and the discontinuous distribution of particle carbides along the grain boundaries before deformation proved conducive to the carbides during the tensile test, as shown in Figure 13A_1 and A_2. Consequently,

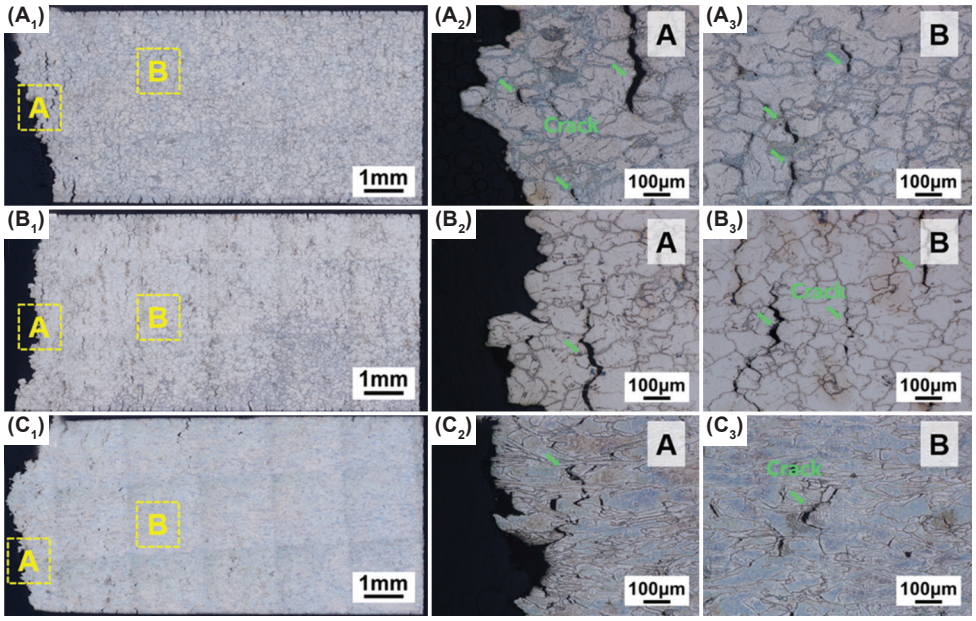

Figure 11. Microstructural morphology of the deformation region failed at high tensile temperature. Results of (A_1-A_3) HIP1100, (B_1-B_3) HIP1180, and (C_1-C_3) HIP1210 specimens. Scale bars: (A1-C1) 1 mm; (A2-C2, A3-C3) 100 μm, magnifications: (A_1-C_1) ×100; (A_2-C_2, A_3-C_3) ×500.
Abbreviation: HIP: Hot isostatic pressing.

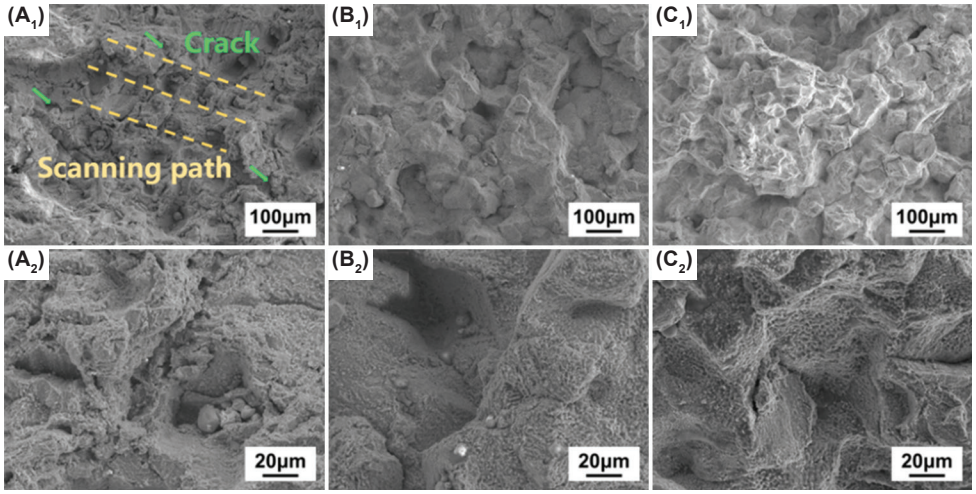

Figure 12. The fracture surface of Hastelloy X tensile specimens failed at high temperatures. Results of (A_1 and A_2) HIP1100, (B_1 and B_2) HIP1180, and (C_1 and C_2) HIP1210 specimens. Scale bars: (A_1-D_1) 100 μm; (A_2-D_2) 20 μm, magnifications: (A_1-D_1) ×500; (A_2-D_2) ×2,500.
Abbreviation: HIP: Hot isostatic pressing.

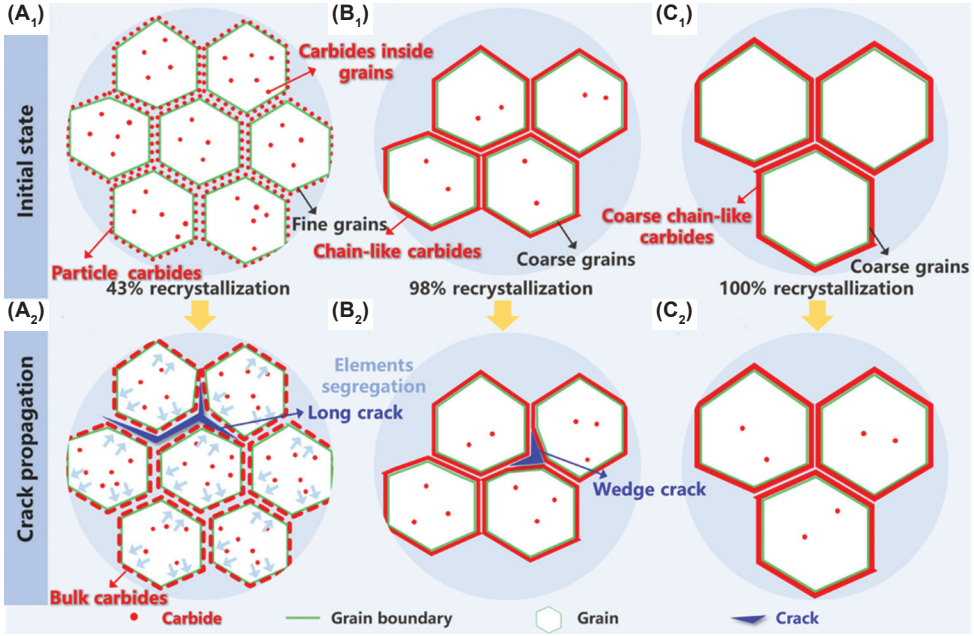

Figure 13. Schematic diagram of high-temperature fracture mechanism. (A_1 and A_2) HIP1100, (B_1 and B_2) HIP1180, and (C_1 and C_2) HIP1210 specimen.
Abbreviation: HIP: Hot isostatic pressing.

the carbides along the grain boundaries significantly coarsened with uneven carbide size after the 900°C tensile test, while the carbides within the grains remained finely dispersed. In contrast, due to the continuous carbide distribution along the grain boundaries before deformation, the carbides in the HIP1180 and HIP1210 specimens precipitated predominantly near the grain boundaries, as shown in Figure 13B_1, B_2, C_1, and C_2. Moreover, only a small number of carbides were observed to be dispersed within the grains.

In contrast to the strengthening effect during room temperature tensile testing, the weakening of grain boundaries occurred during the high temperature tensile test, contributing to differing crack propagation mechanisms in different HIP specimens. During the high-temperature tensile deformation, dislocation pile-up at grain boundaries was alleviated under the combined effect of high temperature and tensile stress,[41] contributing to the reduced strength of the grain boundaries. Therefore, grain boundary sliding and migration became more likely, with

pores preferentially forming in these weakened regions.[42] In the HIP1100 specimen, hard carbides distributed along the grain boundaries were characterized by lower ductility compared to the matrix, contributing to the desynchronized deformation between the carbides and the matrix. Moreover, the large-sized carbides among the discontinuous carbides distributed along the grain boundaries induced localized stress concentrations,[39] making these coarse carbides potential weak regions. Subsequently, cracks were prone to initiate within the bulk carbides and at grain triple junctions, propagating[20] and forming intergranular fracture surfaces and secondary cracks extending along the grain boundaries. In addition, compared to the HIP1180 and HIP1210 specimens, the small-sized grains at HIP1100 resulted in a reduction in the number of grain boundaries, which further exacerbated boundary weakening. This microstructural condition corresponded to reduced tensile strength and elongation, along with the formation of long cracks penetrating the specimens. On the contrary, when the HIP temperature increased to 1,180°C and 1,210°C, the chain-like carbides along the grain boundaries enhanced the strength of the grain boundaries, inhibiting stress concentrations. Moreover, the number of grain boundaries decreased, thereby limiting crack propagation.[22] As a result, the HIP1180 and HIP1210 specimens both achieved improved tensile strength and elongation, attributed to the synergistic effect of reduced number of grain boundaries and chain-like distribution of carbides. These specimens demonstrated fracture morphologies characterized by wedge-shaped cracks and minor cracks, respectively.

4. Conclusion

The microstructure evolution and mechanical properties of LPBF-manufactured Hastelloy X alloy following various HIP treatments at both room and high temperatures were investigated. When the HIP temperature increased from 1,100°C to 1,210°C, the recrystallization process gradually progressed and achieved completion at 1,210°C. The proportion of low-angle grain boundaries decreased from 49.7% at HIP1100 to 4.3% at HIP1180, and eventually to 0% at HIP1210. The carbides along the grain boundaries transformed from particle distribution at HIP1100 to chain-like distribution at HIP1180, and coarse chain-like distribution at HIP1210.

After the HIP treatments, the yield strength decreased, while the tensile strength and elongation increased compared to the as-built specimen. As the HIP temperature increased, the elongation of the HIP specimens gradually improved, reaching a maximum value of 45% at HIP1210. The tensile strength declined, achieving a value of 774 MPa at HIP1100 due to restrained dislocation slip, grain refinement strengthening, and carbide dispersion strengthening.

Compared to the pre-deformation condition, significant carbide coarsening occurred along the grain boundaries in the HIP1100 specimen during high-temperature tensile testing, while minimal changes were observed for the HIP1180 and HIP1210 specimens. As the HIP temperature increased, the tensile strength and elongation both improved due to the synergistic effect of reduced number of grain boundaries and the chain-like distribution of carbides, reaching a maximum tensile strength of 236 MPa and elongation of 29.0% at HIP1210.

Under room temperature tensile testing, the fracture surfaces exhibited typical ductile failure with numerous dimples. In contrast, during high-temperature tensile testing, the cracks primarily propagated along the grain boundaries, with the HIP1210 specimen exhibiting a better capacity for crack inhibition. Compared to the HIP1100 and HIP1180 specimens, the massive feature presented on the fracture surface of HIP1210 was more pronounced, demonstrating a typical characteristic of intergranular fracture.

Acknowledgments

None.

Funding

The research was supported by the National Natural Science Foundation of China (No. 52475332) and the Taishan Scholars Foundation of Shandong Province (No. tsqn202211307).

Conflict of interest

Dr. Swee Leong Sing and Caiwang Tan are the Editorial Board Members of this journal, but were not in any way involved in the editorial and peer-review process conducted for this paper, directly or indirectly. Separately, other authors declared that they have no known competing financial interests or personal relationships that could have influenced the work reported in this paper.

Author contributions

Conceptualization: Junjun Jiang
Data curation: Bingqiu Wang, Yiming Sun, Caiwang Tan
Formal analysis: Caiwang Tan
Investigation: Bingqiu Wang
Methodology: Rongrong Huang, Bo Chen, Caiwang Tan
Resources: Junjun Jiang
Supervision: Rongrong Huang, Bo Chen, Xiaoguo Song
Validation: Linan Xue
Writing – original draft: Bingqiu Wang

Writing – review & editing: Yiming Sun, Xiaohui Zhou, Swee Leong Sing

Ethics approval and consent to participate

Not applicable.

Consent for publication

Not applicable.

Availability of data

All data analyzed have been presented in the paper.

References

1. Pourbabak S, Montero-Sistiaga ML, Schryvers D, Van Humbeeck J, Vanmeensel K. Microscopic investigation of as built and hot isostatic pressed hastelloy X processed by selective laser melting. *Mater Charact*. 2019;153:366-371.

   doi: 10.1016/j.matchar.2019.05.024

2. Iveković A, Montero-Sistiaga ML, Vleugels J, Kruth JP, Vanmeensel K. Crack mitigation in laser powder bed fusion processed hastelloy X using a combined numerical-experimental approach. *J Alloys Compd*. 2021;864:158803.

   doi: 10.1016/j.jallcom.2021.158803

3. Xu L, Gao Y, Zhao L, Han Y, Jing H. Ultrasonic micro-forging post-treatment assisted laser directed energy deposition approach to manufacture high-strength hastelloy X superalloy. *J Mater Proc Technol*. 2022;299:117324.

   doi: 10.1016/j.jmatprotec.2021.117324

4. Blakey-Milner B, Gradl P, Snedden G, *et al*. Metal additive manufacturing in aerospace: A review. *Mater Design*. 2021;209:110008.

   doi: 10.1016/j.matdes.2021.110008

5. Kalender M, Kılıç SE, Ersoy S, Bozkurt Y, Salman S. Additive manufacturing and 3D printer technology in aerospace industry. *2019 9th International Conference on Recent Advances in Space Technologies (RAST)*. 2019. p. 689-694.

   doi: 10.1109/RAST.2019.8767881

6. Yu CH, Peng RL, Lee TL, Luzin V, Lundgren JE, Moverare J. Anisotropic behaviours of LPBF hastelloy X under slow strain rate tensile testing at elevated temperature. *Mater Sci Eng A*. 2022;844:143174.

   doi: 10.1016/j.msea.2022.143174

7. Markovic P, Scheel P, Wróbel R, Leinenbach C, Mazza E, Hosseini E. Cyclic mechanical response of LPBF hastelloy X over a wide temperature and strain range: Experiments and modeling. *Int J Solids Struct*. 2024;305:113047.

   doi: 10.1016/j.ijsolstr.2024.113047

8. Li X, Esmaeilizadeh R, Hosseini E. Microstructure and mechanical response of as-built and solution-annealed LPBF hastelloy X under high-temperature fatigue loading. *Add Manufact Lett*. 2024;10:100227.

   doi: 10.1016/j.addlet.2024.100227

9. Li R, Cheng L, Liu J, *et al*. Modeling and analysis of the mechanical anisotropy of hastelloy X alloy fabricated by laser powder bed fusion. *J Mater Res Technol*. 2024;33:7949-7960.

   doi: 10.1016/j.jmrt.2024.11.148

10. Kong D, Ni X, Dong C, *et al*. Anisotropic response in mechanical and corrosion properties of hastelloy X fabricated by selective laser melting. *Constr Build Mater*. 2019;221:720-729.

    doi: 10.1016/j.conbuildmat.2019.06.132

11. Li C, Liu Y, Shu T, Guan W, Wang S. Effect of solution heat treatment on microstructure, mechanical and electrochemical properties of hastelloy X fabricated by laser powder bed fusion. *J Mater Res Technol*. 2023;24:1499-1512.

    doi: 10.1016/j.jmrt.2023.03.108

12. Liu G, Li B, Zhang S, *et al*. Effect of Fe-based metallic glass on microstructure and properties of hastelloy X manufactured by laser powder bed fusion. *J Alloys Compd*. 2023;966:171561.

    doi: 10.1016/j.jallcom.2023.171561

13. Xie Y, Teng Q, Shen M, *et al*. The role of overlap region width in multi-laser powder bed fusion of hastelloy X superalloy. *Virtual Phys Prototyp*. 2023;18:e2142802.

    doi: 10.1080/17452759.2022.2142802

14. Keshavarzkermani A, Esmaeilizadeh R, Enrique PD, *et al*. Static recrystallization impact on grain structure and mechanical properties of heat-treated hastelloy X produced via laser powder-bed fusion. *Mater Charact*. 2021;173:110969.

    doi: 10.1016/j.matchar.2021.110969

15. Cheng X, Du Z, Chu S, *et al*. The effect of subsequent heating treatment on the microstructure and mechanical properties of additive manufactured hastelloy X alloy. *Mater Charact*. 2022;186:111799.

    doi: 10.1016/j.matchar.2022.111799

16. Ma Q, Dong K, Li F, *et al*. Recent progress in electromagnetic microwave absorption of additively manufactured carbon fiber-reinforced polymer structures. *ESAM*. 2025;1:025160008.

    doi: 10.36922/ESAM025160008

17. Chan YY, Chao Y, Kuo CN. Mechanical properties and energy absorption capability improvement of Ti-6Al-4V porous materials through porous structure design optimization. *ESAM*. 2025;1:025170009.

    doi: 10.36922/ESAM025170009

18. Keller C, Mokhtari M, Vieille B, Briatta H, Bernard P. Influence of a rescanning strategy with different laser powers on the microstructure and mechanical properties of hastelloy X elaborated by powder bed fusion. *Mater Sci Eng A*. 2021;803:140474.

doi: 10.1016/j.msea.2020.140474

19. Montero-Sistiaga ML, Liu Z, Bautmans L, *et al*. Effect of temperature on the microstructure and tensile properties of micro-crack free hastelloy X produced by selective laser melting. *Add Manufact*. 2021;31:100995.

doi: 10.1016/j.addma.2019.100995

20. Agrawal S, Avadhani GS, Suwas S. Deformation behaviour of additively manufactured hastelloy X at high temperatures: The role of concurrent carbide precipitation. *J Alloys Compd*. 2025;1021:179636.

doi: 10.1016/j.jallcom.2025.179636

21. Zheng L, Schmitz G, Meng Y, Chellali MR, Schlesiger R. Mechanism of intermediate temperature embrittlement of Ni and Ni-based superalloys. Crit Rev *Solid State Mater Sci*. 2012;37:181-214.

doi: 10.1080/10408436.2011.613492

22. Han Q, Mertens R, Montero-Sistiaga ML, *et al*. Laser powder bed fusion of hastelloy X: Effects of hot isostatic pressing and the hot cracking mechanism. *Mater Sci Eng A*. 2018;732:228-239.

doi: 10.1016/j.msea.2018.07.008

23. Wang H, Chen L, Dovgyy B, *et al*. Micro-cracking, microstructure and mechanical properties of hastelloy-X alloy printed by laser powder bed fusion: As-built, annealed and hot-isostatic pressed. *Add Manufact*. 2021;39:101853.

doi: 10.48550/arXiv.2011.11003

24. Sanchez-Mata O, Muñiz-Lerma JA, Wang X, *et al*. Microstructure and mechanical properties at room and elevated temperature of crack-free hastelloy X fabricated by laser powder bed fusion. *Mater Sci Eng A*. 2020;780:139177.

doi: 10.1016/j.msea.2020.139177

25. Zhou W, Tian Y, Wei D, *et al*. Effects of heat treatments on the microstructure and tensile properties of IN738 superalloy with high carbon content fabricated via laser powder bed fusion. *J Alloys Compd*. 2023;953:170110.

doi: 10.1016/j.jallcom.2023.170110

26. Yuan Z, Chang F, Chen A, *et al*. Microstructure and properties of SLM-hastelloy X alloy after different hot isostatic pressing + heat treatment. *Mater Sci Eng A*. 2022;852:143714.

doi: 10.1016/j.msea.2022.143714

27. Shaji Karapuzha A, Fraser D, Zhu Y, Wu X, Huang A. Effect of solution heat treatment and hot isostatic pressing on the microstructure and mechanical properties of hastelloy X manufactured by electron beam powder bed fusion. *J Mater Sci Technol*. 2022;98:99-117.

doi: 10.1016/j.jmst.2021.04.059

28. Mani Pandi AS, Senthil Kumar VS. A review: Fabrication techniques of the hastelloy (super alloy) composites and it impacts on the properties. *Mater Today Proc*. 2024.

doi: 10.1016/j.matpr.2024.05.115

29. Qin Y, Liu Y, Guan W, Wang K. Material corrosion characteristics of heat-treated SLM-ed hastelloy X in electrochemical machining process. *Mater Today Commun*. 2024;39:109105.

doi: 10.1016/j.mtcomm.2024.109105

30. Marchese G, Bassini E, Aversa A, *et al*. Microstructural evolution of post-processed hastelloy X alloy fabricated by laser powder bed fusion. *Materials (Basel)*. 2019;12:486.

doi: 10.3390/ma12030486

31. Tomus D, Tian Y, Rometsch PA, Heilmaier M, Wu X. Influence of post heat treatments on anisotropy of mechanical behaviour and microstructure of hastelloy-X parts produced by selective laser melting. *Mater Sci Eng A*. 2016;667:42-53.

doi: 10.1016/j.msea.2016.04.086

32. Li Y, Qi H, Hou H, Lei L. *Effects of Hot Isostatic Pressing on Microstructure and Mechanical Properties of Hastelloy X Samples Produced by Selective Laser Melting*. Netherlands: Atlantis Press; 2017. p. 31-40.

33. Sun S, Teng Q, Xie Y, *et al*. Two-step heat treatment for laser powder bed fusion of a nickel-based superalloy with simultaneously enhanced tensile strength and ductility. *Add Manufact*. 2021;46:102168.

doi: 10.1016/j.addma.2021.102168

34. Liu M, Zeng Q, Hua Y, *et al*. High-temperature tensile properties of hastelloy x produced by laser powder bed fusion with different heat treatments. *Metals*. 2022;12:1435.

doi: 10.3390/met12091435

35. Montero-Sistiaga ML, Pourbabak S, Van Humbeeck J, Schryvers D, Vanmeensel K. Microstructure and mechanical properties of hastelloy X produced by HP-SLM (high power selective laser melting). *Mater Design*. 2019;165:107598.

doi: 10.1016/j.matdes.2019.107598

36. Shu DL, Tian SG, Tian N, Xie J, Su Y. Thermodynamic analysis of carbide precipitation and effect of its configuration on creep properties of FGH95 powder nickel-based superalloy. *Mater Sci Eng A*. 2017;700:152-161.

doi: 10.1016/j.msea.2017.05.108

37. Zhang S, Wang L, Lin X, *et al*. Precipitation behavior of δ phase and its effect on stress rupture properties of selective laser-melted Inconel 718 superalloy. *Compos Part B Eng*.

2021;224:109202.

doi: 10.1016/j.compositesb.2021.109202

38. Zhang S, Lin X, Wang L, *et al*. Strengthening mechanisms in selective laser-melted inconel718 superalloy. *Mater Sci Eng A*. 2021;812:141145.

doi: 10.1016/j.msea.2021.141145

39. Liu M, Zhang K, Liu J, *et al*. High-temperature high cycle fatigue performance of laser powder bed fusion fabricated hastelloy X: Study into the microstructure and oxidation effects. *Mater Design*. 2024;243:113037.

doi: 10.1016/j.matdes.2024.113037

40. Sun Y, Huang R, Lin D, *et al*. Investigation of deformation mechanisms in hastelloy X superalloy manufactured via laser powder-bed fusion: Insights into effects of carbides and cellular structure at elevated temperatures. *J Manufact Processes*. 2023;108:165-179.

doi: 10.1016/j.jmapro.2023.10.083

41. Wu S, Dai SB, Heilmaier M, *et al*. The effect of carbides on the creep performance of hastelloy X fabricated by laser powder bed fusion. *Mater Sci Eng A*. 2023;875:145116.

doi: 10.1016/j.msea.2023.145116

42. Marchese G, Basile G, Bassini E, *et al*. Study of the microstructure and cracking mechanisms of hastelloy X produced by laser powder bed fusion. *Materials (Basel)*. 2018;11:106.

doi: 10.3390/ma11010106